Source analysis of the M_w 6.3 2004 Al Hoceima earthquake (Morocco) using regional apparent source time functions

Daniel Stich[1] and Flor de Lis Mancilla
Instituto Andaluz de Geofísica, Universidad de Granada, Granada, Spain

David Baumont
Institut de Radioprotection et de Sûreté Nucléaire, Fontenay-aux-Roses, France

Jose Morales
Instituto Andaluz de Geofísica, Universidad de Granada, Granada, Spain

Received 7 August 2004; revised 22 February 2005; accepted 14 March 2005; published 11 June 2005.

[1] We use small and moderate aftershocks of the 24 February 2004 Al Hoceima earthquake as empirical Greens' functions (EGFs) to retrieve the rupture history of the main event. The magnitude, depth, and geometry of faulting were estimated for the main shock and 20 small and moderate aftershocks (M_w between 3.9 and 5.2) computing moment tensor solutions. For the main shock, we obtain a moment magnitude of $M_w = 6.3$ and a nearly pure double-couple source (4% compensated linear vector dipole) with predominately strike-slip faulting. The preferred fault plane has a strike of N11°E, a dip of 72°, and a rake of −17°. Fourteen aftershocks, having depths (±4 km) and faulting geometries (±11° for the strike of the preferred plane) similar to the ones found for the main event, were used as EGFs. Apparent source time functions (ASTFs) of the Al Hoceima event were retrieved at twelve regional stations using an iterative time domain deconvolution on the *P* waveforms. At each station, time functions are enhanced by stacking of the deconvolved waveforms for different EGFs. ASTFs show total durations of 5 to 6 s, two consecutive subevents separated by about 3 s, and only a weak effect of directivity. We further investigate the source history by inverting the set of ASTFs for the distribution of fault slip and rupture propagation. Two different source models were selected for presentation, one involving one single fault plane and the other involving two parallel fault planes. The two-fault model fits more accurately the observations and leads to a more plausible slip distribution. We estimate rupture dimensions of about 10 × 10 km^2 and 8 × 8 km^2 and moment magnitudes of M_w = 6.2 and 6.0 for the first and second subevent, respectively.

Citation: Stich, D., F. Mancilla, D. Baumont, and J. Morales (2005), Source analysis of the M_w 6.3 2004 Al Hoceima earthquake (Morocco) using regional apparent source time functions, *J. Geophys. Res.*, *110*, B06306, doi:10.1029/2004JB003366.

1. Introduction

[2] In the night of 24 February 2004, a major earthquake hit the area around the city of Al Hoceima, on the Mediterranean coast of Morocco. According to news reports, the earthquake caused 628 casualties, and more than 2500 buildings collapsed. The epicenter was located about 10 km south of Al Hoceima near the village of Aït Kamra, and near real-time waveform evaluation indicated a moment magnitude of M_w = 6.4 (European-Mediterranean Seismological Center, EMSC, http://www.emsc-csem.org). No surface expression of the main rupture plane has been identified in the source region, but surface fissures with small, centimeter-scale offset are observed over an almost 20 km long zone [*Aït Brahim et al.*, 2004].

[3] The Al Hoceima region is located near the eastern termination of the Alpine Rif mountain belt and is considered as the seismically most active area in Morocco [*Calvert et al.*, 1997]. Tectonic deformation of northern Morocco is related to the oblique NW-SE convergence between the African and Eurasian plates [*DeMets et al.*, 1994]. The predominant faulting style along most of the Mediterranean Moroccan margin and Alboran sea is strike-slip faulting [e.g., *Mezcua and Rueda*, 1997; *Bezzeghoud and Buforn*, 1999; *Stich et al.*, 2003a], contrasting with predominately reverse faulting in adjacent regions along the African-Eurasian plate boundary in northern Algeria and the western Atlantic Ocean. While in the Atlantic Ocean and northern Algeria, seismicity focuses rather sharply around the African-Eurasian plate boundary, no linear boundary can be traced over the Moroccan-Iberian section of the plate contact

[1] Now at Istituto Nazionale di Geofisica e Vulcanologia, Bologna, Italy.

0148-0227/05/2004JB003366$09.00

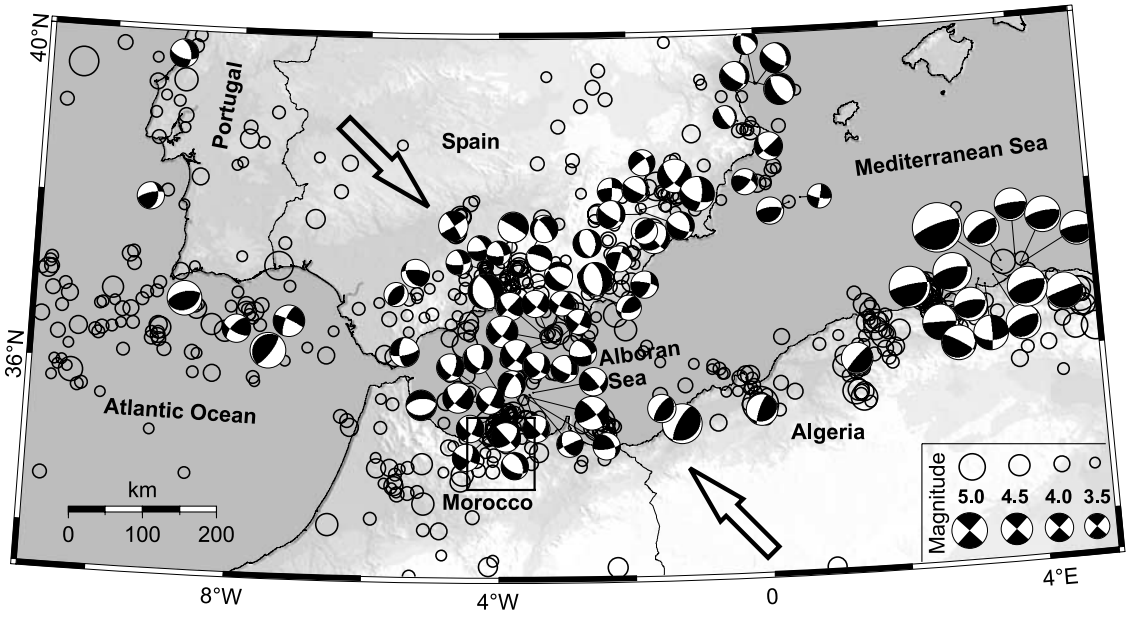

Figure 1. Seismicity along the Moroccan-Iberian section of the African-Eurasian plate boundary. Circles show earthquakes epicenters for events with $m_b \geq 3.5$ for the period 1982 to 2002 (USGS/NEIC data file http://neic.usgs.gov). Seismicity does not mark a linear plate boundary between Morocco and Spain. Arrows show the direction of plate convergence, at a rate of ~4 mm/yr [*DeMets et al.*, 1994]. Focal mechanisms are taken from the Instituto Andaluz de Geofísica moment tensor catalogue (http://www.ugr.es/~iag/tensor/) for the period 1984–2003 and show the predominant strike-slip faulting style along most of the Moroccan Mediterranean margin and Alboran sea. The box shows the position of the map in Figure 3.

(Figure 1). The contact between northwestern Africa and Spain is characterized by distributed deformation and diffuse seismicity within a ~400 km wide zone, extending well into northern Morocco and southern Spain. Small and moderate magnitude events ($M_w < 5.5$) dominate seismicity. Between 0°W and 8°W, only four magnitude 6+ events occurred over the last 100 years, including a $M_w = 6.1$ earthquake in 1910 near Adra at the Spanish coast [*Stich et al.*, 2003b], a $m_b = 7.1$, deep focus earthquake beneath Granada, Spain, in 1954 [*Chung and Kanamori*, 1976], a $M_w = 6.6$ earthquake just west of the Strait of Gibraltar in 1964 [*Pondrelli et al.*, 1999], and a $M_w = 6.0$ earthquake on 26 May 1994 near Al Hoceima in the immediate proximity of the 2004 shock [*Calvert et al.*, 1997; *Bezzeghoud and Buforn*, 1999]. Available hypocenter locations and the macroseismic intensity patterns suggest that the 1994 and 2004 Al Hoceima earthquakes ruptured different faults, with the 2004 event possibly situated 10 km southeastward of the 1994 event [*El Alami et al.*, 1998; *Jabour et al.*, 2004; *Aït Brahim et al.*, 2004].

[4] The 2004 Al Hoceima main shock was followed by an extensive aftershock sequence, including four events with magnitude 5+ according to the EMSC data file (http://www.emsc-csem.org). No foreshock is reported. The Al Hoceima earthquake is the first major seismic event along the Moroccan-Iberian section of the African-Eurasian plate boundary, which was recorded at a dense regional network of high-resolution, broadband seismographs. Recent upgrading of the MedNet network (installation of RTC) and IAG network (installation of SESP, HORN and ASCB) were on time for that earthquake. We choose 20 regional broadband stations in Spain, Portugal, and Morocco for this study, twelve of them at epicentral distances of less than 400 km. We perform (1) time domain moment tensor inversions to estimate depth, magnitude, and orientation of faulting for the main shock and the major aftershocks, (2) empirical Greens' functions analysis to estimate source time functions for the main shock (appropriate Green's functions are chosen according to moment tensor estimates, and source time functions at each station are enhanced by stacking the results for the individual aftershocks), and (3) inversion of the apparent source time functions for the spatial and temporal pattern of the Al Hoceima main shock rupture.

2. Moment Tensor Solutions

[5] Near real-time moment tensor estimates for the Al Hoceima main shock were made available by various agencies, including Harvard University, U.S. Geological Survey (USGS), Italian Istituto Nazionale di Geofisica e Vulcanologia (INGV), Swiss Eidgenössisch Technische Hochschule (ETH)-Zürich, and Spanish Instituto Geográfico Nacional (IGN). They used several different data sets and different methodological approaches [*Dziewonski and Woodhouse*, 1983; *Sipkin*, 1994; *Pondrelli et al.*, 2002; *Bernardi et al.*, 2004; *Rueda and Mezcua*, 2005]. Moment tensor focal mechanisms show predominately strike-slip faulting style, with the left-lateral nodal plane striking NNE-SSW and the right-lateral nodal plane striking ESE-WNW. Varying minor fractions of reverse or normal fault slip appear in individual solutions. Al Hoceima aftershocks are more than one magnitude smaller than the main shock,

Table 1. Elastic Parameters of the Average, Plane-Layered Lithospheric Model Used for Inverting Intermediate-Period Waveforms[a]

z, km	v_P, km/s	v_S, km/s	ρ, g/cm^3
2	5.40	3.10	2.50
12	6.10	3.51	2.75
12	6.40	3.68	2.85
6	6.90	3.94	2.90
50	8.10	4.60	3.30
100	8.10	4.40	3.35
∞	8.20	4.70	3.40

[a]The parameter z is the layer thickness.

and close to the magnitude threshold of those routine moment tensor projects that use long-period waveforms. Three and two aftershock moment tensors were given by INGV and ETH-Zürich, respectively. IGN provided real-time moment tensor estimates for 15 aftershocks, using intermediate-period waveforms at three stations with azimuthal coverage less than 50°. Most aftershock moment tensors resemble the orientation and the strike-slip faulting style of the main event mechanism.

[6] We use an extensive data set from near-regional broadband stations, to obtain estimates of focal mechanisms, depths and magnitudes for earthquakes of the Al Hoceima sequence. The main shock and 32 small and moderate aftershocks between 24 February and 16 April have been selected for the analysis, based on data quality at the stations of the regional network. We perform time domain, linear inversion for the first-order deviatoric seismic moment tensor, using full three-component, intermediate-period displacement waveforms. The best solution is defined by the least squares minimum of misfit between the observed seismograms and synthetic Greens' function predictions [*Langston et al.*, 1982]. All inversions are performed for temporal and spatial point sources. A careful manual tuning of weighting factors for the individual traces was done to improve the azimuthal balance of the data, reduce the influence of noisy traces, and obtain an overall improvement of waveform fits. A more detailed description of the processing scheme is given by *Stich et al.* [2003a].

[7] Greens' functions were computed with a reflection matrix code [*Randall*, 1994] for an average, one-dimensional (1-D) lithospheric model with four crustal layers and a Moho depth of 32 km (Table 1). The Earth model merges results mainly from refraction and wide-angle reflection seismic profiling [*ILIHA–DSS Group*, 1993], and receiver function studies [*Julià and Mejía*, 2004] in the Hercynian continental crust of the Iberian Peninsula. This model approximates average crustal properties over the Ibero-Maghrebian region, and it has been shown that it predicts with good accuracy propagation effects for intermediate-period waveforms (>20 s) for most regional wave paths. It has been used previously to obtain moment tensors for earthquake sources at the Mediterranean Moroccan margin [*Stich et al.*, 2003a]. For the 2004 Al Hoceima sequence, all waveforms are filtered between 20 and 50 s period to allow an appropriate and consistent treatment of propagation effects. Filtering in this passband introduces a threshold magnitude for moment tensor inversion of about $M_w = 4.0$ for this source region, below which the signal-to-noise ratio becomes low at most regional stations. The locations of the main shock and the aftershocks were provided by the IGN (IGN data file; http://www.mfom.es/ign). The hypocenter depth was not fixed for the linear moment tensor inversion, since depth estimates are not well constrained from regional network recordings. Instead, 15 equidistant trial depths between 2 and 30 km were tested successively. So the global misfit minimum of inversion and grid search returns both an estimate of moment centroid depth and seismic moment tensor. To calibrate absolute travel times for *P* waves, observed seismograms and Green's functions are aligned using the picked first (usually *Pn*) arrivals in the velocity recordings, and the ray theoretical first arrivals in the synthetics. For the main shock, a delay of 3 s was introduced into the synthetics to simulate a generic centroid time shift for a magnitude 6+ event.

[8] We obtain stable moment tensor estimates for the main shock ($M_0 = 2.9 \times 10^{18}$ N m, $M_w = 6.3$) and 20 small and moderate aftershocks (M_w between 3.9 and 5.2, Table 2). This set is expected to be complete down to magnitude $M_w = 4.2$, except for the first few hours after the main shock, when intermediate-period recordings are still dominated by coda waves. The accumulated seismic moment of aftershocks in Table 2 is $M_0 = 2.0 \times 10^{17}$ N m, and the total moment release during the aftershocks sequence should not exceed 10% of the main shock seismic moment. The inverted moment tensor sources predict with good accuracy the main characteristics of the observed intermediate-period waveforms (Figure 2), except for transversely polarized waves traveling across, or close to, the Arc of Gibraltar toward stations in western Andalusia and Portugal. Also modeling is less accurate for station RTC in western Morocco, probably due to wave propagation along strike of the Rif mountain chain, where the lithospheric structure may introduce 3-D propagation effects, which we do not account for in Green's function computation. All moment tensor solutions are clearly dominated by double-couple force systems. The nondouble-couple part is less well resolved from moment tensor inversion, and absorbs some of the effects of noise, location errors and model inaccuracies. The average component of compensated linear vector dipoles is 11%, and for no event the compensated linear vector dipole (CLVD) component exceeds 29%.

[9] The Al Hoceima main shock shows strike-slip faulting with a minor normal component, and a nearly double-couple moment tensor (4% CLVD). The formally best combination of moment tensor and depth is obtained at 14 km. Our preferred fault plane solution is the left-lateral N11°E oriented nodal plane (dip of 72° and rake of −17°), since this orientation coincides with the strike of the dominant neotectonic lineaments south of Al Hoceima (Figure 3). The approximately NNE-SSW faults have been shown to be active in aftershock studies of the 1994 Al Hoceima earthquake [*Calvert et al.*, 1997; *El Alami et al.*, 1998] and microseismic surveys [*Medina*, 1995]. They form a dense network of subparallel synthetic strike-slip faults on the northwestern block of the NE-SW striking Nekor fault. The present-day tectonic deformation of the eastern Rif seems to be accommodated mainly on this network of subsidiary faults, resulting in a diffuse distribution of seismicity, while no significant seismicity is reported on the Nekor fault itself [*Calvert et al.*, 1997]. The pattern of surface fissures observed after the earthquake is consistent

Table 2. Moment Tensor Solutions for the Al Hoceima Main Shock and Major Aftershocks[a]

			DC Plane 1			DC Plane 2						
	Date	Time, UT	Strike	Dip	Rake	Strike	Dip	Rake	z, km	CLVD, %	M_0, N m	M_w
MS	24 Feb.	0227:46	11	72	−17	107	73	−161	14	3.8	2.88e+18	6.3
A1	24 Feb.	1104:44	19	61	−26	123	67	−148	16	13.1	3.29e+15	4.3
A2	24 Feb.	1642:12	11	68	−7	104	83	−157	10	7.1	1.69e+15	4.1
A3	24 Feb.	1853:02	12	85	−40	106	49	−173	10	13.1	1.26e+15	4.0
A4	24 Feb.	2037:02	3	76	−15	97	74	−165	16	25.2	1.06e+15	4.0
A5	25 Feb.	0521:14	0	69	−4	92	86	−158	14	13.5	4.73e+15	4.4
A6	25 Feb.	1244:54	14	77	−16	108	73	−167	10	18.3	6.91e+16	5.2
A7	25 Feb.	1633:28	22	73	−16	117	73	−162	10	5.0	1.10e+15	4.0
A8	26 Feb.	1207:03	13	75	−9	105	80	−165	16	9.3	2.45e+16	4.9
A9	27 Feb.	0059:00	8	81	−19	102	71	−170	14	11.1	4.04e+15	4.4
A10	27 Feb.	0312:36	10	73	−5	102	84	−163	12	23.1	3.13e+15	4.3
A11	27 Feb.	1650:42	16	74	−10	110	80	−163	14	16.5	6.22e+15	4.5
A12	28 Feb.	1629:25	36	35	23	287	77	123	4	1.5	2.36e+15	4.2
A13	2 March	2036:26	13	79	−25	109	65	−167	12	28.4	4.12e+15	4.4
A14	7 March	0637:52	2	81	−8	93	81	−171	22	0.3	3.76e+16	5.0
A15	10 March	0422:18	354	68	−50	109	44	−148	6	2.3	1.14e+15	4.0
A16	12 March	1721:51	352	49	−62	134	47	−118	6	9.6	2.20e+16	4.9
A17	15 March	1239:13	9	65	−39	119	54	−148	12	8.8	7.17e+14	3.9
A18	20 March	0937:26	20	77	−34	119	56	−164	10	5.6	7.34e+15	4.5
A19	1 April	0025:35	28	53	14	289	79	142	8	9.7	1.33e+15	4.0
A20	6 April	0153:09	110	33	160	216	79	59	6	9.5	2.38e+15	4.2

[a]MS, main shock; A1–A20, aftershocks. Date and origin time are taken from the IGN data file (www.mfom.es/ign). The faulting geometry is described by the fault angles of the double-couple nodal planes (strike, dip, and rake) and the contribution of a compensated linear vector dipole (CLVD) to the solution (in percent). Nodal planes 1 are our preferred fault planes. We select the ~N11°E planes for the strike-slip events (see text) and in each case the steeper dipping plane for the normal faulting events (A15, A16) and the shallower dipping plane for the reverse events (A12, A19, A20). Read 2.88e+18 as 2.88×10^{18}.

with left-lateral strike-slip movement along a NNE-SSW oriented plane [*Aït Brahim et al.*, 2004], and also the damage pattern supports that orientation (M. Feriche and F. Vidal, unpublished manuscript, 2004). The strike of the right-lateral nodal plane (N107°E) does not coincide with the trend of major neotectonic lineaments.

[10] Most aftershock moment tensor mechanisms strongly resemble the main shock solution, showing predominately strike-slip faulting with minor normal components (Figure 3). The preferred left-lateral fault planes are subparallel for all 15 strike-slip solutions, with strike values varying from N0°E to N22°E, dip values from 61° to 85°, and rake values from −4° to −40°. Noticeably, the scatter of fault angle parameters is nearly symmetrical for these solutions, and data can be fit approximately by a normal distribution (Figure 4). The standard deviations of the inverted fault angle parameter (6° for strike and dip and 11° for the rake) are of the same order or less than expected moment tensor inaccuracies, as introduced by the inversion of noise, location inaccuracy, as well as varying recording geometries and weighting factors for the individual inversions. Consequently, from regional seismological data alone, we cannot distinguish between strictly parallel faults for all strike-slip events, or actual near-normal distributions of fault angle parameters that might reflect properties of the fault network and the probability of failure for individual structures.

[11] Further, two normal faulting mechanisms (A15 and A16, M_w = 4.0 and 4.9) and three reverse faulting mechanisms (A12, A19 and A20, M_w between 4.0 and 4.2) were obtained. The normal and reverse solutions correspond to fundamentally different waveforms compared to strike-slip events and are well constrained by the data. The normal faulting mechanisms are located about 25 km south of the main shock, in the area of the NNW-SSE trending Jbel Hammam normal fault system (Figure 3) and consistent with previous focal mechanism solutions in the area [*Medina*, 1995]. The reverse faulting solutions are located closer to the main shock and must be considered unusual in the Al Hoceima region. They may have been triggered by stress transfer onto ancient compressive structures in the vicinity of the main shock rupture surface. Depth estimates for aftershocks range from 4 to 16 km, except for one event (A14 at 22 km). The gross depth distribution agrees with results from local earthquake studies, which indicate a lower limit of seismicity near the base of the upper crust at about 14 km depth [*Hatzfeld et al.*, 1993; *Calvert et al.*, 1997]. Finally, we want to report our notion that, for this source region, centroid depths may be slightly overestimated from regional moment tensor inversion using the average 1-D lithospheric model.

[12] The predominately strike-slip faulting style of the main shock and most aftershocks coincides with previous focal mechanisms reported for northern Morocco and the Alboran Sea [e.g., *Medina*, 1995, *Mezcua and Rueda*, 1997; *Bezzeghoud and Buforn*, 1999; *Stich et al.*, 2003a]. Principal *P* axes are oriented about NNW-SSE for all events, with a mean azimuth of N330°E and just minor scatter between N309°E and N351°E. This is consistent with an NNW-SSE orientation of the maximum horizontal stress proposed in a previous study [*Medina*, 1995]. The inverted moment tensor mechanisms show a clearly different orientation compared to focal mechanisms in the Alboran Sea, where *P* axes are oriented nearly N-S [*Mezcua and Rueda*, 1997; *Stich et al.*, 2003a]. Those N-S *P* axes in the Alboran Sea differ from the regional NW-SE reference direction of plate convergence, which points to a major anomaly of the stress field within the thinned continental crust of the Alboran basin.

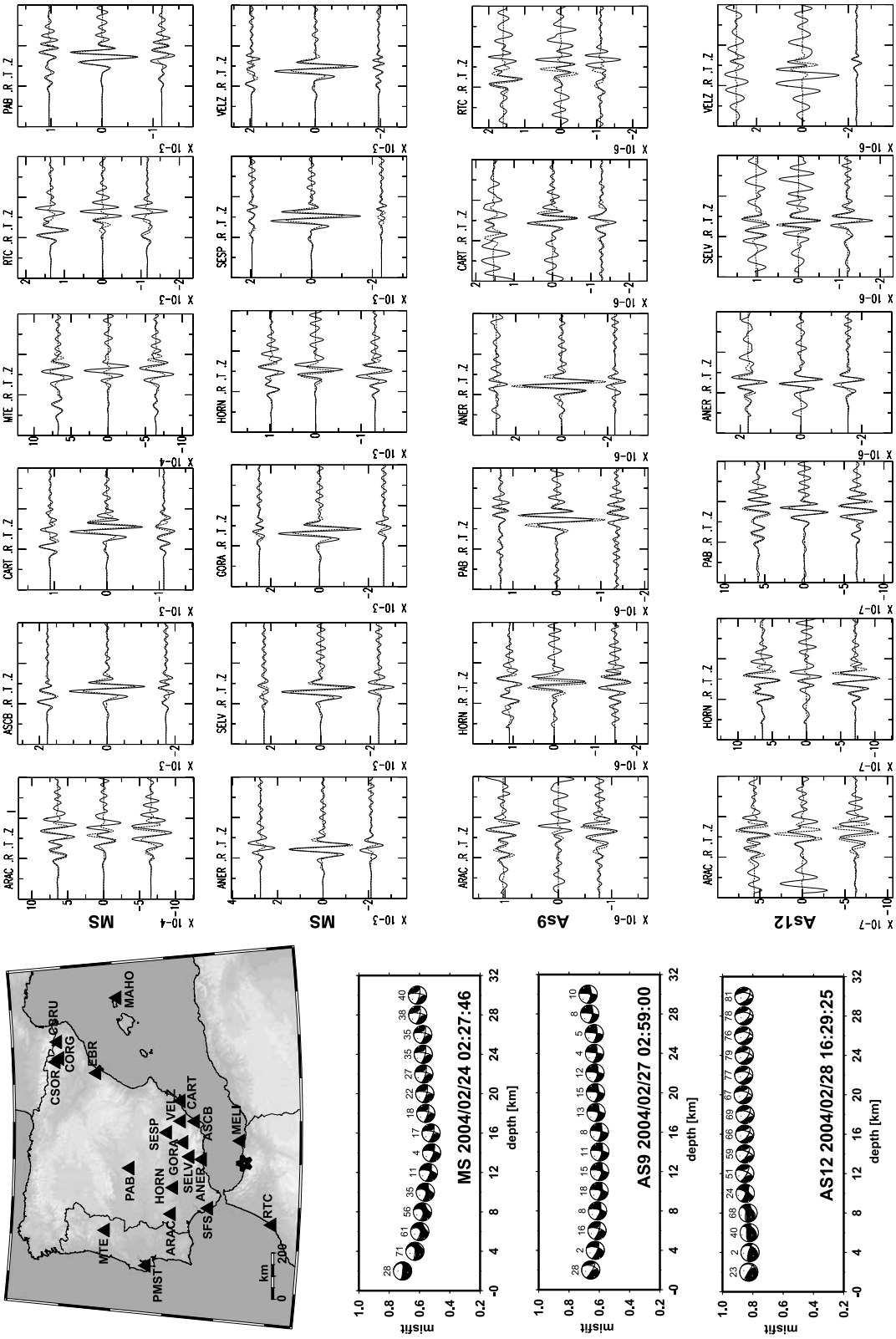

Figure 2. Sample waveform fits from moment tensor inversion for the Al Hoceima main shock (MS) and two aftershocks (AS9, M_w = 4.4, with mechanism similar to the main shock, and AS12, M_w = 4.2, with predominately reverse faulting mechanism). The boxes show, from top to bottom, radial, transverse, and vertical intermediate-period waveforms. Solid lines correspond to observed waveforms, and dashed lines correspond to the moment tensor predictions. All waveforms have duration of 300 s. Vertical axes scale is meters. Map shows the distribution of all stations used for moment tensor inversion. Star marks the epicenter of the main shock. Below, L2 misfit versus depth diagrams are given for the three examples, illustrating the variations of misfit, mechanism and CLVD component (small numbers above the beach balls) with depth for 15 equidistant trial depth between 2 and 30 km.

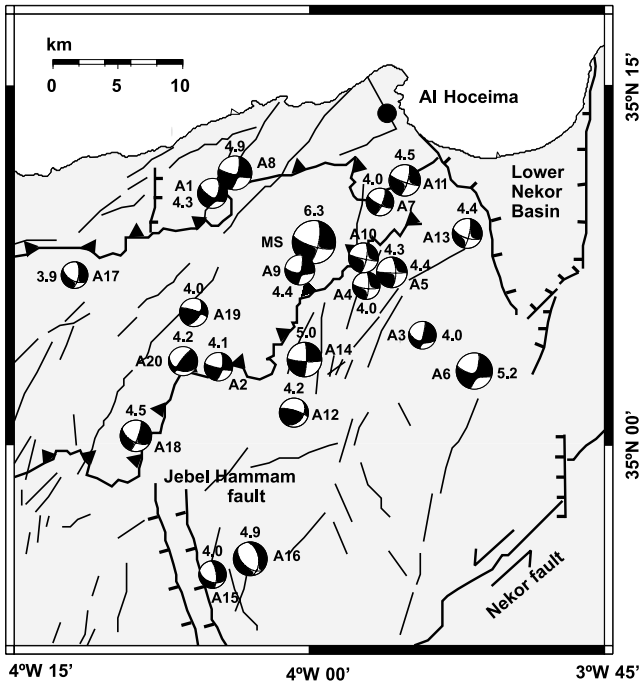

Figure 3. Moment tensor mechanisms for the Al Hoceima main shock (MS) and major aftershocks (A1–A20) in lower hemisphere projection. Deviatoric moment tensor estimates, including both double-couple component (thin nodal lines) and nondouble-couple remainder, are displayed. The event ID according to Table 1 is labeled at each mechanism. Events A9 and A4 have been shifted slightly from their original location for displaying purpose. Neotectonic faults are redrawn from *Calvert et al.* [1997]. Thick lines mark major faults, and thin lines mark subsidiary faults. Most moment tensors can be attributed to a network of approximately NNE-SSW striking, subsidiary, left-lateral strike-slip faults in the source area.

Focal mechanism data from the Al Hoceima region suggest that the anomalous faulting pattern does not extend beyond the Moroccan Mediterranean margin.

3. Apparent Source Time Functions

[13] For the Al Hoceima main shock, intermediate-period waveforms can be modeled adequately with a double-couple point source. Source finiteness and potential rupture complexity should have more pronounced effects on shorter-period waveforms comparable to the timescale of the source process. In this section we analyze broadband *P* waveforms to reveal the time function of moment release during the main shock rupture. At regional distances, an accurate simulation of propagation effects for broadband *P* waves is beyond the capabilities of available lithospheric models for the complex Betic-Rif-Alboran region. Instead we use empirical Green's functions to approximate the impulse response of the earth and isolate the source time function from the seismograms [*Hartzell*, 1978]. A small event, which shares nearly identical radiation pattern, path and site effects with the main event, but lacks a relevant signature of source finiteness, can be seen as an empirical Greens' function. Thus an aftershock can be considered as a valuable calibration event, when its location and focal mechanism are similar to the ones of the main event. We select a set of 14 aftershocks that are likely to fulfill these conditions according to the results of moment tensor inversion. This selection includes those aftershocks that show strike-slip mechanisms and depth estimates similar to the main event (depths from 10 to 16 km). Evaluating the entire set of aftershocks will allow us to a posteriori discriminate potentially inappropriate calibration events, and to improve the quality of the source time functions by stacking.

[14] Apparent source time functions (ASTFs) at each station are obtained from the main shock recordings by deconvolution of empirical Greens' functions. We apply an iterative time domain technique that synthesizes the deconvolved function as a superposition of Gaussian pulses [*Ligorría and Ammon*, 1999; *Kikuchi and Kanamori*, 1982]. Within each iteration, the position and amplitude of the current pulse is found by cross correlation of the main shock and aftershock seismograms, the pulse is added to the source time function, and the corresponding prediction is subtracted from the main shock seismogram. The series is truncated after 200 iterations. The time domain approach generates a causal source time function, and avoids intrinsic numerical instabilities of spectral division in frequency domain deconvolution. Especially for smaller Al Hoceima aftershocks, the low signal-to-noise ratio at several regional stations would require relatively high water level constants to stabilize frequency domain deconvolution, which may cause a distortion of the deconvolved function [*Velasco et al.*, 1995]. The Gaussian pulse width was adjusted to assure that frequencies above the corner frequency of the aftershocks are suppressed. Amplitude spectra of the largest

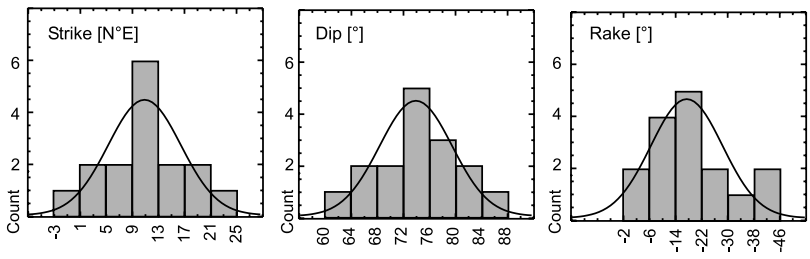

Figure 4. Histograms of fault angle parameters for the left-lateral nodal plane of 16 strike-slip moment tensor solutions (main shock and 15 aftershocks). Normal distributions (solid curves) adequately fit the data with mean values of strike N11°E, dip 74°, and rake −18° (see discussion in text). Data were binned in intervals about 2/3 the standard deviation (i.e., 4° bins for strike and dip and 8° bins for rake).

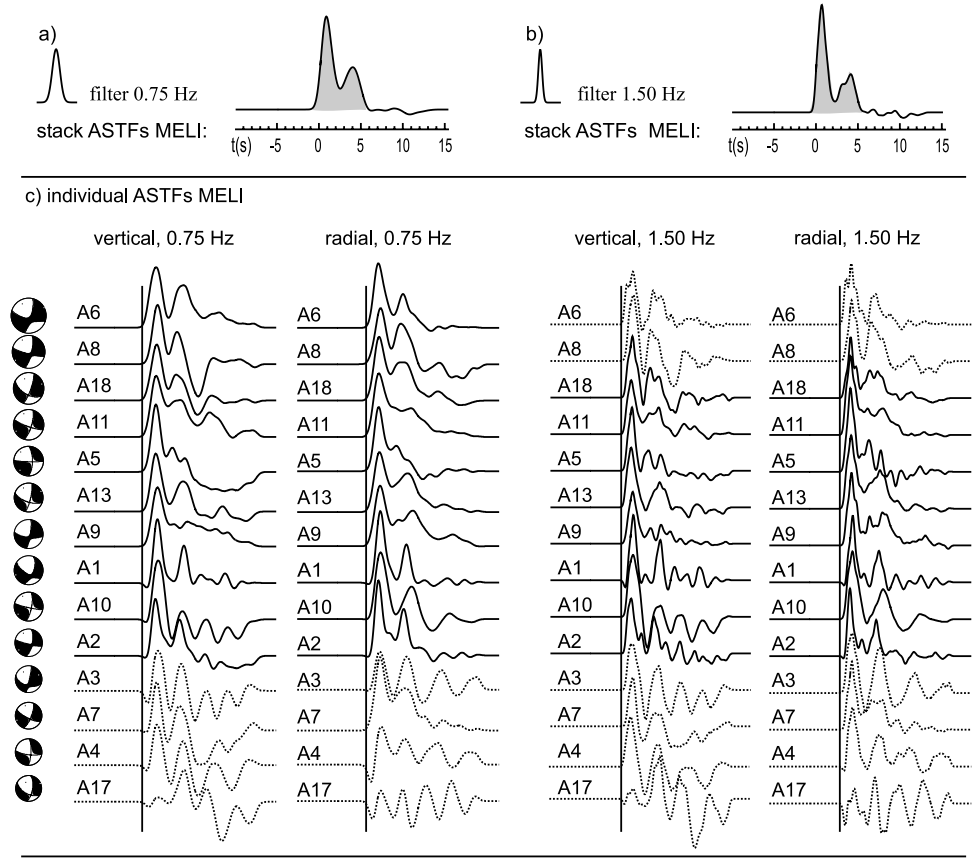

Figure 5. (a, b) Average apparent source time functions (ASTFs) at stations MELI, obtained from stacking the deconvolved source time functions for individual aftershocks and components. Different Gaussian filters are tested in source time function retrieval (see text). The corresponding Gaussian pulses, used to construct the time functions, are shown to the left of the deconvolution result. (c) ASTFs for individual empirical Greens' functions, i.e., vertical and radial components of the different aftershocks, with two different Gaussian filters. Time functions are sorted in order of decreasing seismic moment of the aftershocks, the corresponding moment tensor mechanism is shown to the left, and the event ID according to Table 2 is labeled at the traces. Dotted time functions do not contribute to the stacking results in Figures 5a and 5b.

aftershock (A6 and A8, $M_w \approx 5$) indicate corner frequencies just below 1 Hz, so we choose a Gaussian low-pass filter that drops to a gain of 0.1 at 0.75 Hz. The corresponding Gaussian pulse width in the time domain, and hence the resolution of the deconvolved time function, is about 1.1 s (at half the total height of the pulse). Deconvolution is performed for radial and vertical components of *P* waves, using time windows from 10 to 40 s duration according to the epicentral distance. Only recordings with *P* arrival picking accuracy better than 0.2 s are used for the analysis, since time domain deconvolution is sensitive to the alignment of the main shock and aftershock seismograms. No positivity constraint was introduced in deconvolution to permit that random noise can cancel out during stacking.

[15] We start discussing the results at station MELI, which recorded high-quality seismograms for most studied aftershocks. An average ASTF at this station was estimated by stacking the unit area deconvolved functions for ten individual aftershocks with magnitude $M_w \geq 4.1$ (Figure 5). The average time function shows a total duration of 6 s, and two clear peaks indicating two consecutive episodes of moment release. The two pulses are broader than the individual Gaussian pulses used to construct the time function, so their waveforms reflect finite source properties. To check if we missed fundamental source heterogeneities slightly shorter than the selected pulse duration, a Gaussian low pass at 1.5 Hz was tested to increase the bandwidth of the source time function. Then the average ASTF was estimated by stacking the deconvolved functions only for smaller (M_w 4.1 to 4.5) empirical Greens' functions. This alternative time function (Figure 5b) is very similar to the previous result (Figure 5a), but the total source duration appears slightly shorter (5.5 s), giving an idea of pulse broadening caused by the 0.75 Hz Gaussian filter used in the initial source time function calculation. Nevertheless, we will consistently use the 0.75 Hz filter for the rest of the recordings, because we depend on including the two $M_w \approx 5$ aftershocks at the more distant stations, where smaller aftershocks have low signal-to-noise ratio.

[16] The individual deconvolved functions at station MELI consistently show a first peak with short risetime (Figure 5c). A second, smaller peak is evident in all wave-

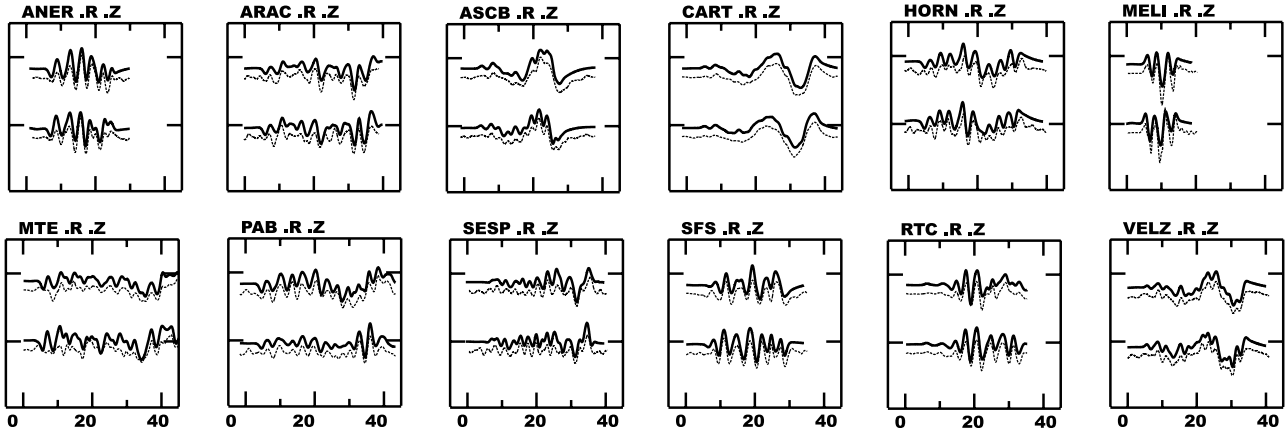

Figure 6. Sample waveform fits between the observed *P* wave train (solid lines) and the predictions from deconvolution (ASTF convolved with EGF, dashed lines). Observations are filtered with a 0.75 Hz Gaussian low pass to match the frequency content of the traces. Note that the fits do not correspond to stacked, average ASTFs (which cannot be related to a particular EGF) but fits to the deconvolution of one individual aftershock only. We show deconvolutions on vertical and radial *P* waves for aftershocks A6.

forms, but shape and duration vary among the individual deconvolutions. A third pulse between 6 s and 9 s after the first arrival appears in several time functions (e.g., A18, A11), but is contradicted by simultaneous negative pulses in other time functions (e.g., A5, A10). These contributions cancel out completely during stacking, which leads us to rejecting the third pulse as a spurious feature below the noise level of the individual deconvolved functions. Thus stacking must be considered a crucial step to obtain reliable results for these data. Different from the individual ASTFs, the stacked, average ASTF drops to near-zero values after termination of the second pulse (<5% of the peak amplitude), which evidences an efficient suppression of any kind of artifacts. The individual deconvolved functions are of varying quality, which we try to assess using two criteria: (1) similarity between individual and stacked time function, and (2) lack of prominent negative amplitudes that, for an appropriate Greens' function, would indicate backward slip along the fault, which is not a plausible source process. A decrease of time function quality with decreasing aftershock moment is clearly visible, but we cannot identify any significant correlation with aftershock source mechanism, epicenter position, or depth. Especially depth difference was initially expected to be a crucial parameter. Synthetic modeling indicates that the depth difference between aftershock and main shock centroids should not exceed about ±4 km, in order to permit a satisfactory recovery of the source time function for a corner frequency of 0.75 Hz. For larger depth differences the interference of depth phases may cause artifacts like negative pulses, pulse duplication, distorted risetime or apparently longer source duration. For the selected set of aftershock recordings, however, the observations point to the signal-to-noise ratio as the single most important quality criteria.

[17] ASTFs at other regional stations were retrieved in the same way. Individual ASTFs were excluded from the stack when they show obvious deficiencies, like large negative pulses, negative onset, high noise level, or if the deconvolution procedure does not converge to a good fit of the main shock waveform. Sample waveform fits for the largest aftershock A6 are given in Figure 6. For each station, we can keep between 5 and 14 waveforms for stacking, except for stations very close to the nodal plane of the main shock mechanism (SELV, GORA), where we were not able to obtain reliable time functions from *P* wave observations. The average ASTFs at 11 remaining regional broadband stations show a two-peak structure similar to the results for MELI (Figure 7). Both peaks have similar duration of about 3 s, and the peak-to-peak delay times are about 3 s, too.

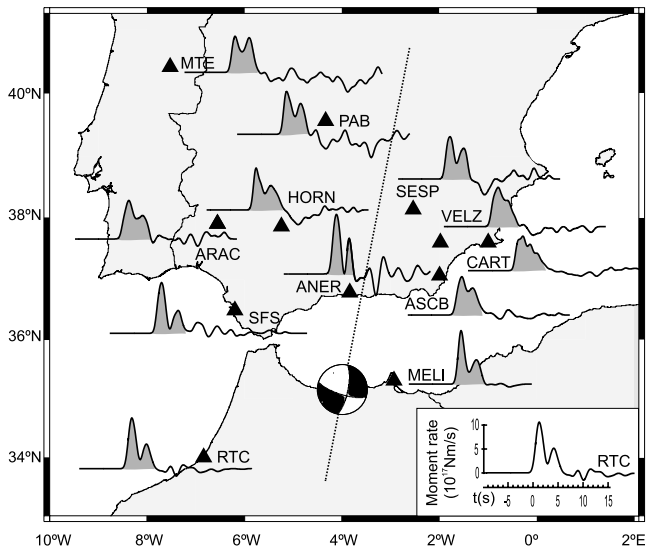

Figure 7. Stacked, average ASTFs at 12 regional stations. The dashed line shows the strike of the preferred fault plane of the Al Hoceima main shock mechanism. We attribute a lower quality to the ASTF at the near-nodal station ANER. The area of all time functions is scaled to the total moment release. The inlay shows vertical and horizontal scale for one example function. ASTFs show two episodes of mayor moment release, a total duration between 5 and 6 s and peak moment rates around 1×10^{18} N m/s. Though the overall duration is slightly shorter at the northern stations, the individual subevents lack a significant effect of horizontal rupture directivity.

ASTFs were all normalized using the seismic moment value we inferred (2.9×10^{18} N m). Peak moment rates are near 1×10^{18} N m/s. The first pulse releases about 65% of the total seismic moment, or 1.9×10^{18} N m, and the second one is 1×10^{18} N m. This corresponds to moment magnitudes M_w of 6.2 and 6.0, respectively. The total duration of the apparent time functions varies slightly between 5 s and 6 s, with slightly shorter durations at the northward stations (SESP, ANER, PAB) compared to stations east and west of the epicenter (MELI, RTC, SFS).

4. Kinematic Rupture Parameters

[18] As shown in section 3, two consecutive episodes of moment release can be identified in the apparent source time functions (ASTFs). This strongly suggests that the rupture of the Al Hoceima event was heterogeneous. ASTFs retrieved at stations well distributed in azimuth capture the rupture process from different angles of observation, so these data may allow evaluating, for instance, the extent and duration of the rupture, the rupture velocity, and the spatial distribution of total fault slip [e.g., *Ammon et al.*, 1993; *Courboulex et al.*, 1998]. We attempt to further characterize the rupture history of this earthquake by inverting our best ASTFs, using the nonlinear, damped least squares iterative inversion scheme described by *Baumont et al.* [2002].

[19] Our fault model is a N11°E plane, dipping from the surface to the ESE with an angle of 72° (Figure 8a). The fault model dimensions were fixed to 26×18 km^2. We assumed a nucleation point at 10 km depth, a bit shallower than the centroid estimate from moment tensor analysis, and well within the seismogenic layer according to previous studies [*Hatzfeld et al.*, 1993; *Calvert et al.*, 1997]. The exact position of the nucleation point does not significantly affect the result. The fault model was regularly discretized using a 2×2 km^2 mesh. The kinematic model parameters (slip amplitude, rupture time, and risetime) are defined for each grid element, and are constrained to be within physically reasonable intervals ($0 \leq$ slip ≤ 1.5 m; $0.5 \leq$ risetime ≤ 5 s; $2.5 \leq$ rupture velocity ≤ 3.2 km/s). A correlation length of 5 km, slightly above the resolution that we may expect from a $M_w = 5$ empirical Green's functions, was introduced to smoothen the rupture pattern through the correlation matrix on the model parameters. To be consistent with the parameterization used in the ASTFs calculations, we model the ASTFs as the superposition of Gaussian pulses radiated from each grid element [*Baumont et al.*, 2002]. The shear modulus was fixed to $3.4 \cdot 10^{10}$ N/m^2, in agreement with shear velocity and density in the source layer (compare Table 1).

[20] Travel time delays are assigned to the individual grid elements for an upper crustal *P* wave velocity of 6.1 km/s, and for the ray geometry of direct *P* arrivals, which depart from the source region nearly horizontal. At near-regional distances, direct *P* waves dominate our deconvolution results. This can be verified by particle motion plots in the vertical radial plane of wave propagation, where the largest amplitudes correspond to ray parameters of about 0.16 to 0.17 s/km, indicating nearly horizontal wave propagation in the source layer. The combination of subhorizontal takeoff angles and steep dip of the fault plane makes the down dip variation of travel time delays small (<0.05 s/km) and reduces the vertical sensitivity of the slip inversion. *S* wave observations, with smaller phase velocity, could provide a slightly better resolution, but this is hampered by the larger picking inaccuracy of *S* arrivals (>0.5 s for most waveforms). An attempt to retrieve reliable apparent time functions from *P* wave observations at far-regional distances, for which waves travel through the upper mantle and leave the source volume rather steeply, failed due to the low quality of aftershock waveforms. Thus only near-regional *P* waves were considered in our inversion. On the basis of data quality and azimuthal distribution, we select eight apparent source time functions for the inversion (Figure 8e), covering an azimuthal range of 200° around the epicenter. A 10% a priori error was applied on the data. Several inversions were performed testing various homogeneous starting models. Similar results were obtained for the slip distributions and to a lesser extent for the risetime distribution, but it clearly appears that the rupture velocity distribution was poorly constrained. We thus fixed the rupture velocity by trial and error, retaining the most appropriate values for fitting the ASTFs (2.7–3.1 km/s).

[21] Figure 8 shows one of our best kinematic models obtained for a rupture velocity of 2.9 km/s. This model gives an adequate overall fit to the observed ASTFs (RMS = 4.5%), reproducing the two subevents and their respective peak amplitudes. The seismic moment released by this model ($M_0 = 2.7 \times 10^{18}$ N m) is close to the target M_0. The first pulse observed in the ASTFs corresponds to a compact slip patch of 10×10 km^2, with a maximum slip between 0.8 and 1.0 m in the central part and an average risetime of 1 s. The second pulse is generated by two or three distinct slip patches located near the upper and lower edge of the fault model. This slip distribution during the later stage of the rupture process appears peculiar and contradicts external constraints: It would imply that important seismic slip occurs below the base of the seismogenic layer as deduced from the depth distribution of local earthquakes (about 14 km [*Hatzfeld et al.*, 1993; *Calvert et al.*, 1997]). Moreover, the high slip amplitudes predicted near the surface north of the epicenter, close to the coastline, are contradicted by the absence of major surface rupture or particularly high intensities in that area (M. Feriche and F. Vidal, unpublished manuscript). The use of a larger correlation length (10 km) does not affect the main features of the slip but removes the NNE deeper contributions. Several alternative fault models of smaller dimensions were tested, resulting in slip concentrations close to the upper and lower limits of the fault model, exceeding 1 m locally. In order to further qualify the robustness of the main features of the slip distribution, we performed a stochastic exploration of the model space (for more details, see *Baumont et al.* [2004]) and retained about 1500 models with a RMS lower than 5.5%. The corresponding predicted ASTFs are shown in Figure 8e (cloud of solid gray lines). To highlight the coherent features of the slip distributions, the models were low-pass filtered (10 km cutoff wavelength) and both the lowest and mean values were reported at each grid point (Figure 8d). This analysis shows that the compact slip patch near the nucleation point and its deeper tail are rather well constrained, whereas the relative locations of the shallow and deep NNE slip patches are more poorly resolved. The inverted rupture pattern reflects directly the properties of

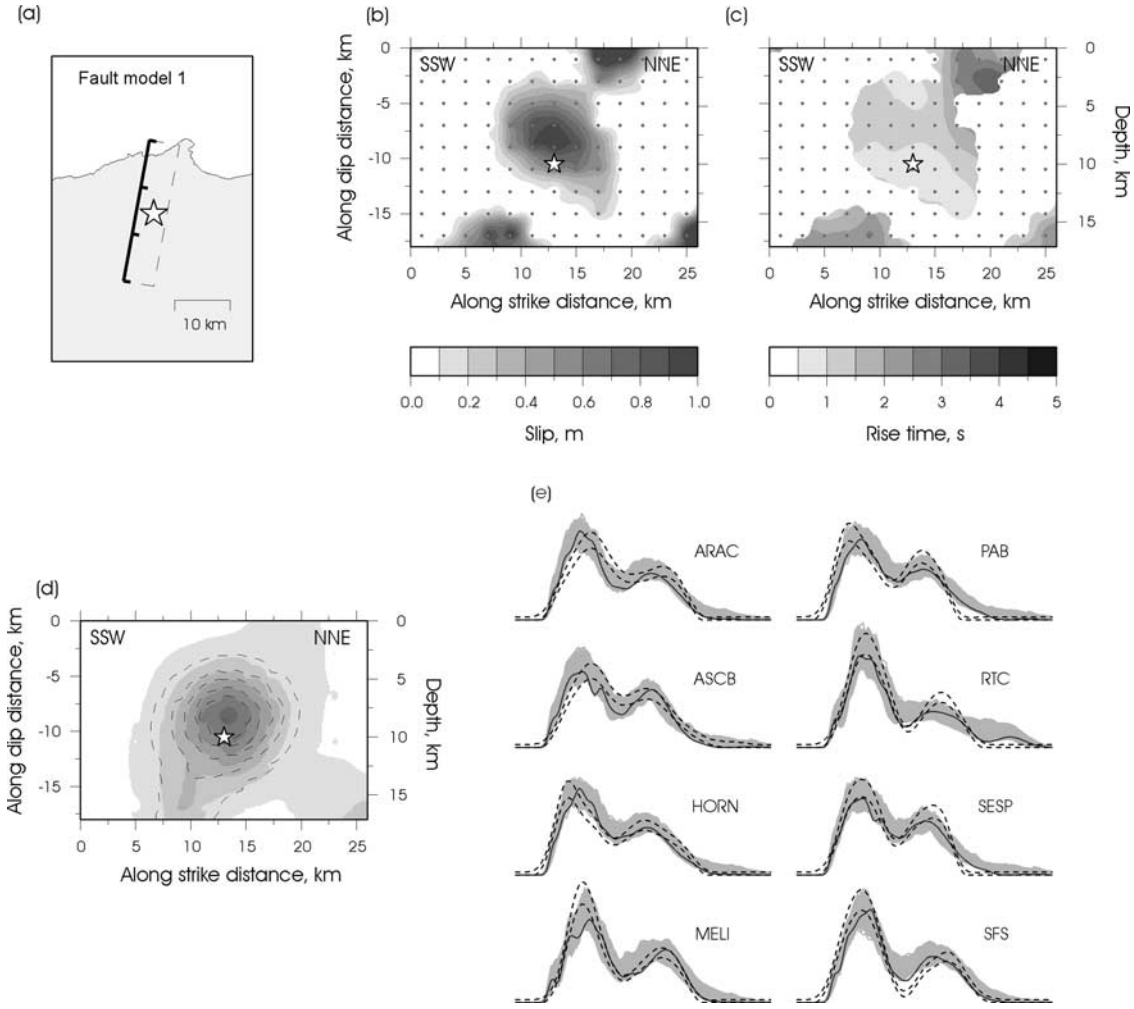

Figure 8. (a) Kinematic rupture model for the M_w 6.3, 2004 Al Hoceima earthquake inverted from regional *P* waves ASTFs on a N11°E single fault. We assumed a constant 2.9 km/s rupture velocity and fixed the depth of the nucleation point (star) to 10 km. (b, c) One of our best slip and risetime distributions. (e) Predicted ASTFs (solid dark lines) reproduced satisfactorily well (with an RMS of 4.5%) the two pulses of the estimated ASTFs (dashed dark lines corresponding to a 10% a priori error). The ASTFs predicted for stochastically generated models (see text) are also shown (cloud of solid gray lines). Notice the presence in our best model of (1) a large slip patch below the base of the seismogenic layer and (2) of some significant slip near the surface. These features are only weakly sensitive to the starting model used (here a 10 cm homogeneous slip) and to the rupture velocity. (d) Robustness analysis based on a stochastic exploration of the model space (1500 models with a RMS lower than 5.5% were retained). The selected models were low-pass filtered (10 km cutoff wavelength). Both the lowest (0.1 m contour lines) and mean (shaded gray areas) slip values were reported. The robustness analysis shows that the compact slip patch near the nucleation point and its deeper tail are rather well constrained, the relative locations of the shallow and deep NNE slip patches being more poorly resolved. The details of the risetime distribution are not well constrained; however, the inner values are overall found to be close to 1 s, whereas the outer values are close to 2 s.

this second pulse, which appears remarkably similar and compact at all stations, while the main shock rupture front had already propagated more than 6 km at that time. This should introduce large travel time delays and pulse broadening into the ASTFs. This paradox can be played down formally in inversion by a preference of near-vertical rupture propagation, where travel time delays are smallest, which explains the resulting slip distribution.

[22] We introduce an alternative fault model that attributes the second subevent to the activation of a second fault plane, instead of a second episode of outward propagating rupture. This model will result in a smaller extent of the rupture front near the end of the rupture process. *Ihmlé* [1998] pointed out that both geometries may generate similar apparent time functions, as long as the instantaneous moment centroids roughly coincide. A linear master event relocation scheme [e.g., *Fitch*, 1975] was applied to infer the relative position of the moment centroid of the second fault patch from the azimuthal variations of peak-to-peak delaytimes in the source time functions. To better constrain

the relative depths of the two subevents, far-regional ASTFs were added, although we consider them less reliable because they were obtained using only one aftershock (A6, the largest one). We select stations where one single phase dominates the *P* wave window, i.e., the *sP* phase at ARSA, Austria (distance 19°, azimuth N44°E, delay time 2.5 s) and the *pP* phase at EIL, Israel (distance 33°, azimuth N88°E, delay time 2.6 s, waveforms not shown). The second subevent was relocated 0.7 km shallower than the first one, and at 1.6 km to the SW, with a delay of 2.9 s. However, standard errors of the relative location are comparable to the model parameters and actual centroid distance is poorly resolved (0 to 3 km). A well-studied example of a strike-slip earthquake that ruptured parallel and conjugate fault branches is the 1999 Hector Mine earthquake [e.g., *Hauksson et al.*, 2002; *Ji et al.*, 2002]. For the Al Hoceima earthquake, we assume identical focal mechanisms and parallel faults for both subevents. This is supported by the strong similarity among all strike-slip moment tensor solutions for aftershocks, the predominant orientation of faults in the source area, and by the nearly pure double-couple force system of the composite moment tensor, which implies some similarity of both subevent moment tensor mechanisms.

[23] Our alternative fault model is composed of two parallel faults with hypocenters shifted in time and space according to the results of the relative relocation between the centroid positions (Figure 9a). The best value of rupture velocity was found to be 3.1 km/s for this model. As shown in Figure 9, the two-fault model fits the ASTFs slightly better (RMS = 3.2%). The first subevent is characterized by a predominately upward propagation of the rupture front starting at 10 km depth and dying out near the surface (Figure 9b). The rupture covers a 10×10 km^2 area, with an average and maximum slip values of 0.5 and 1 m, respectively. The risetime distribution, although it is weakly constrained, is relatively homogenous with values close to 1 s (Figure 9c). The second subevent, corresponding in this model to the activation of a parallel fault located to the SW, is characterized by a slightly asymmetric up-northward propagation of the rupture front (Figure 9d). This event ruptured an 8×8 km^2 area, with an average and maximum slip values of 0.3 and 0.6 m, respectively. The risetime distribution (Figure 9e) appears to be more heterogeneous, with an average value larger (2 s) than the values obtained for the first event. The stress drop values are equal to about 3 MPa for both subevents. The total seismic moment is slightly underpredicted (2.7×10^{18} instead of 2.9×10^{18} N m). Several tests were performed considering various rupture velocities, and starting models, and a robustness analysis based on the stochastic exploration of the model space was performed (Figures 9f and 9g). Whereas similar characteristics of slip distributions were obtained, especially predominately symmetric rupture patterns for both subevents, the risetime distributions appeared to be more poorly constrained.

[24] No surface rupture is predicted in the two-fault model and the vertical extent of the rupture is smaller than the presumed thickness of the seismogenic layer in the source region, so that no exotic source process must be invoked to explain the observations. Given a slightly better fit to the ASTFs, a smoother slip pattern, and the more credible rupture distribution compared to external constraints, the two-fault model is our preferred source model. The partitioning of main shock slip on two nearby faults, as well as the apparently diffuse distribution of aftershocks (compare Figure 3), both point to distributed deformation within an extended source volume. Finally we recall that the second subevent lacks a significant effect of directivity, and report that it can be fitted well assuming rupture along the auxiliary WNW-ESE plane, however this orientation is not supported by local tectonics. Also the activation of a conjugate fault branch is unlikely, since no aftershock moment tensor indicates activity on a conjugate fault system. Evaluating the available evidence, we propose that the Al Hoceima main shock ruptured two nearby, parallel faults, activated with a $\sim$3 s time delay, and characterized by moment magnitudes M_w of 6.2 and 6.0 respectively.

5. Summary

[25] The 24 February 2004 Al Hoceima earthquake and its aftershock sequence are recorded at a dense regional network of broadband seismographs. We isolate the signature of source finiteness from near-regional seismograms, using an empirical Greens' function technique. In a previous step, we determine moment tensor solutions for the Al Hoceima sequence to facilitate an appropriate selection of aftershocks for the analysis. Fourteen aftershocks show similar mechanisms and centroid depths as the main event. These mechanisms show predominately strike-slip faulting style and steeply dipping nodal planes. On the basis of macroseismic and seismotectonic criteria, our preferred fault planes are the left-lateral, NNE-SSW oriented nodal planes. Fault angle parameters of these planes have mean values of strike N11°E, dip 74° and rake −18°, and standard deviation smaller than 11°. To obtain apparent source time functions (ASTFs) at regional stations, the empirical Greens' functions were deconvolved from the main shock recordings using an iterative time domain approach. We synthesize the apparent source time functions as a series of Gaussian pulses, which are low-pass filtered at 0.75 Hz to allow the use of the largest aftershocks in the analysis. For the nearest station MELI, we could verify that ASTFs are similar in the 0.75 Hz limited band, as well as in a 1.5 Hz limited band when derived from smaller aftershocks with higher resolving power. We stack the individual ASTFs for each station. This is a crucial step to improve the quality and reliability of source time functions.

[26] The characteristics of the ASTFs are similar at all regional stations, showing two consecutive peaks of major moment release and a total duration of about 5.5 s. We invert ASTFs for the slip distribution and find some incompatibility with a continuously propagating rupture front in a single-fault model. Especially, the second pulse shows similar shape at all stations, and a very abrupt termination, which is inconsistent with a large spatial extent of the rupture front during the late stage of the rupture process. We obtain a more plausible slip distribution and slightly better fits to the ASTFs with a source model involving two parallel faults side by side, and two distinguishable earthquakes of moment magnitudes M_w 6.2 and 6.0. This geometry is supported by the similarity among aftershock mechanisms, and local tectonics comprising distributed shear and a dense network of subparallel NNE-SSW

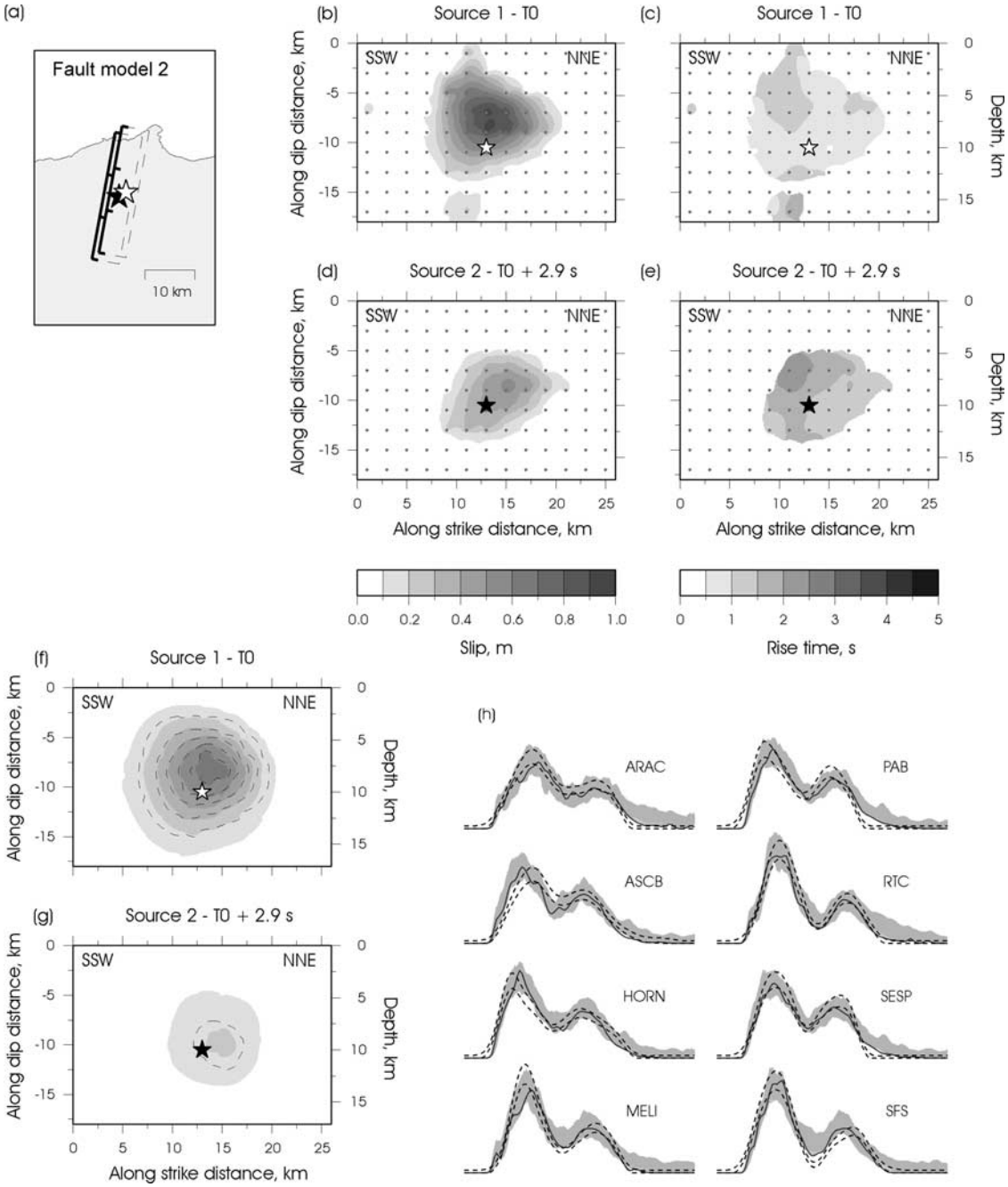

Figure 9. (a) Kinematic rupture model for the M_w 6.3, 2004 Al Hoceima earthquake inverted from regional *P* waves ASTFs on two parallel, N11°E faults. The relative location of the two faults (open star for the first event, solid star for the second event) and the 2.9 s nucleation delay are based on the relative relocation of peak-to-peak pulses delays picked on the ASTFs (see text). The best rupture model was obtained using a 3.1 km/s rupture velocity, although this value is not tightly constrained. Best slip and risetime distributions (b, c) for the first event and (d, e) for the second event. Notice that in this model, the slip dies out toward the surface and no slip was inferred below the base of the seismogenic layer. (h) Predicted ASTFs (dark solid lines) reproduced well both the timing and amplitudes of the estimated ASTFs (dark dashed lines) with an RMS of 3.2%. ASTFs predicted for the stochastically generated models are also shown (solid gray lines). (f, g) Robustness analysis (see legend of Figure 8) showing that the main characteristics of the slip distribution are rather well constrained.

faults. The distance between the two active faults was estimated as 1.5 km according to the azimuthal variations of peak-to-peak delaytimes in the source time functions, and the delay of the second earthquake as 2.9 s. Slip inversion indicates a rupture surface of 10×10 km^2 and maximum slip close to 1 m for the first event and a rupture of 8×8 km^2 and maximum slip close to 0.6 m for the second event. The estimation of average stress drop is 3 MPa.

[27] **Acknowledgments.** This study was possible thanks to the efforts in collecting high-quality broadband data at many networks and institutes: IAG, Geofon, MedNet, IRIS, Spanish Real Observatorio de la Armada, Universidad Complutense de Madrid, Institut Cartográfic de Catalunya and Observatori de l'Ebre, Portuguese Instituto Superior Técnico, Geophysical Institute of Israel, and Austrian Zentralanstalt für Meteorologie und Geodynamik. Part of the data was retrieved using the Wilber tool at ORFEUS. We are grateful for the detailed comments of Jirí Zahradník, Helene Lyon-Caen, and an anonymous reviewer, which greatly helped us to sharpen the discussion. We appreciate discussions on the results of a field survey in the epicentral area with Mercedes Feriche and Paco Vidal. Chuck Ammon and George Randall provided program codes for this study. We acknowledge work on free software SAC [*Goldstein et al.*, 1999] and GMT [*Wessel and Smith*, 1998]. We received financial support by the Spanish DGI projects REN2002-04198-C02-01/RIES and CGL2005-04541-C03-01, MEC grant EX2004-0489, by UE-FEDER, and by the research group RNM104 of Junta de Andalucía.

References

Aït Brahim, L., C. Nakhcha, B. Tadili, A. El Mrabet, and N. Jabour (2004), Structural analysis and interpretation of the surface deformations of the February 24th, 2004 Al Hoceima earthquake, *Newsletter 21*, pp. 10–12, Eur.-Mediter. Seismol. Cent., Bruyères-le-Châtel, France.

Ammon, C. J., A. A. Velasco, and T. Lay (1993), Rapid estimation of rupture directivity: Application to the 1992 Landers (M_s = 7.4) and Cape Mendocino (M_s = 7.2), California earthquakes, *Geophys. Res. Lett.*, *20*, 97–100.

Baumont, D., F. Courboulex, O. Scotti, N. S. Melis, and G. Stavrakakis (2002), Slip distribution of the M_w 5.9, 1999 Athens earthquake inverted from regional seismological data, *Geophys. Res. Lett.*, *29*(15), 1720, doi:10.1029/2001GL014261.

Baumont, D., O. Scotti, F. Courboulex, and N. Melis (2004), Complex kinematic rupture of the M_w 5.9, 1999 Athens earthquake as revealed by the joint inversion of regional seismological and SAR data, *Geophys. J. Int.*, *158*, 1078–1987.

Bernardi, F., J. Braunmiller, U. Kradolfer, and D. Giardini (2004), Automatic regional moment tensor inversion in the European-Mediterranean region, *Geophys. J. Int.*, *157*, 703–716.

Bezzeghoud, M., and E. Buforn (1999), Source parameters of the 1992 Melilla (Spain, M_w = 4.8), 1994 Alhoceima (Morocco, M_w = 5.8), and 1994 Mascara (Algeria, M_w = 5.7) earthquakes and seismotectonic implications, *Bull. Seismol. Soc. Am.*, *89*, 359–372.

Calvert, A., F. Gomez, D. Seber, M. Barazangi, N. Jabour, A. Ibenbrahim, and A. Demnati (1997), An integrated geophysical investigation of recent seismicity in the Al-Hoceima region of north Morocco, *Bull. Seismol. Soc. Am.*, *87*, 637–651.

Chung, W., and H. Kanamori (1976), Source process and tectonic implications of the Spanish deep-focus earthquake of March 29, 1954, *Phys. Earth Planet. Inter.*, *13*, 85–96.

Courboulex, F., M. A. Santoyo, J. F. Pacheco, and S. K. Singh (1998), The 14 September 1995 (M = 7.3) Copala, Mexico, earthquake: A source study using teleseismic, regional, and local data, *Bull. Seismol. Soc. Am.*, *87*, 999–1010.

DeMets, C., R. G. Gordon, D. F. Argus, and S. Stein (1994), Effects of recent revisions to the geomagnetic reversal time scale on estimates of current plate motion, *Geophys. Res. Lett.*, *21*, 2191–2194.

Dziewonski, A. M., and J. H. Woodhouse (1983), An experiment in the systematic study of global seismicity: Centroid moment-tensor solutions for 201 moderate and large earthquakes of 1981, *J. Geophys. Res.*, *88*, 3247–3271.

El Alami, S. O., B. Tadili, T. E. Cherkaoui, F. Medina, M. Ramdani, L. Aït Brahim, and M. Harnafi (1998), The Al Hoceima earthquake of May 26, 1994 and its aftershocks: A seismotectonic study, *Ann. Geophys.*, *41*, 519–537.

Fitch, T. J. (1975), Compressional velocity in source regions of deep earthquakes: An application of the master event technique, *Earth Planet. Sci. Lett.*, *135*, 156–166.

Goldstein, P., D. Dodge, and M. Firpo (1999), SAC2000: Signal processing and analysis tools for seismologists and engineers, in *International Handbook of Earthquake and Engineering Seismology*, part B, edited by W. Lee et al., Elsevier, New York.

Hartzell, S. H. (1978), Earthquake aftershocks as Green's functions, *Geophys. Res. Lett.*, *5*, 1–4.

Hatzfeld, D., V. Caillot, T. E. Cherkaoui, H. Jebli, and F. Medina (1993), Microearthquake seismicity and fault plane solutions around the Nekor strike-slip fault, Morocco, *Earth Planet. Sci. Lett.*, *120*, 31–41.

Hauksson, E., L. M. Jones, and K. Hutton (2002), The 1999 M_w 7.1 Hector Mine, California, earthquake sequence: Complex conjugate strike-slip faulting, *Bull. Seismol. Soc. Am.*, *92*, 1154–1170.

Ihmlé, P. F. (1998), On the interpretation of subevents in teleseismic waveforms: The 1994 Bolivia deep earthquake revisited, *J. Geophys. Res.*, *103*, 17,919–17,932.

ILIHA–DSS Group (1993), A deep seismic sounding investigation of the lithospheric eterogeneity and anisotropy beneath the Iberian Peninsula, *Tectonophysics*, *221*, 35–51.

Jabour, N., M. Kasmi, M. Menzhi, A. Birouk, L. Hni, Y. Hahou, Y. Timoulali, and S. Badrane (2004), The February 24th, 2004 Al Hoceima earthquake, *Newsletter 21*, pp. 7–10, Eur.-Mediter. Seismol. Cent., Bruyères-le-Châtel, France.

Ji, C., D. J. Wald, and D. V. Helmberger (2002), Source description of the 1999 Hector Mine, California, earthquake, part II: Complexity of slip history, *Bull. Seismol. Soc. Am.*, *92*, 1208–1226.

Julià, J., and J. Mejía (2004), Thickness and V_p/V_s ratio variation of the Iberian crust, *Geophys. J. Int.*, *156*, 59–72.

Kikuchi, M., and H. Kanamori (1982), Inversion of complex body waves, *Bull. Seismol. Soc. Am.*, *72*, 491–506.

Langston, C. A., J. S. Barker, and G. B. Pavlin (1982), Point-source inversion techniques, *Phys. Earth Planet. Inter.*, *30*, 228–241.

Ligorría, J. P., and C. J. Ammon (1999), Iterative deconvolution and receiver-function estimation, *Bull. Seismol. Soc. Am.*, *89*, 1395–1400.

Medina, F. (1995), Present-day state of stress in northern Morocco from focal mechanism analysis, *J. Struct. Geol.*, *17*, 1035–1046.

Mezcua, J., and J. Rueda (1997), Seismological evidence for a delamination process in the lithosphere under the Alboran Sea, *Geophys. J. Int.*, *129*, 1–8.

Pondrelli, S., G. Ekström, A. Morelli, and S. Primerano (1999), Study of source geometry for tsunamigenic events of the Euro-Mediterranean area, in *International Conference on Tsunamis*, pp. 297–307, U.N. Educ., Sci., and Cult. Organ., Paris.

Pondrelli, S., A. Morelli, G. Ekström, S. Mazza, E. Boschi, and A. M. Dziewonski (2002), European-Mediterranean regional centroid-moment tensors: 1997–2000, *Phys. Earth Planet. Inter.*, *130*, 71–101.

Randall, G. E. (1994), Efficient calculation of complete differential seismograms for laterally homogeneous Earth models, *Geophys. J. Int.*, *118*, 245–254.

Rueda, J., and J. Mezcua (2005), Near real-time seismic moment tensor determination in Spain, *Seismol. Res. Lett.*, in press.

Sipkin, S. A. (1994), Rapid determination of global moment-tensor solutions, *Geophys. Res. Lett.*, *21*, 1667–1670.

Stich, D., C. J. Ammon, and J. Morales (2003a), Moment tensor solutions for small and moderate earthquakes in the Ibero-Maghreb region, *J. Geophys. Res.*, *108*(B3), 2148, doi:10.1029/2002JB002057.

Stich, D., J. Battló, J. Morales, R. Macià, and S. Dineva (2003b), Source parameters of the 1910 M_w = 6.1 Adra earthquake (southern Spain), *Geophys. J. Int.*, *155*, 539–546.

Velasco, A. A., C. J. Ammon, and T. Lay (1995), Source time function complexity of the great 1989 Macquarie Ridge earthquake, *J. Geophys. Res.*, *100*, 3989–4009.

Wessel, P., and W. H. F. Smith (1998), New, improved version of the Generic Mapping Tools released, *Eos Trans. AGU*, *79*, 579.

D. Baumont, Institut de Radioprotection et de Sûreté Nucléaire, B.P. 17, F-92262 Fontenay-aux-Roses, France. (david.baumont@irsn.fr)

F. Mancilla and J. Morales, Instituto Andaluz de Geofísica, Universidad de Granada, E-18071 Granada, Spain. (flor@iag.ugr.es; morales@iag.ugr.es)

D. Stich, Istituto Nazionale di Geofisica e Vulcanologia, Via Donato Creti 12, I-40128 Bologna, Italy. (daniel@bo.ingv.it)